

# Valley polarization transition driven by biaxial strain in Janus GdClF monolayer

San-Dong Guo<sup>1</sup>, Xiao-Shu Guo<sup>1</sup>, Xiu-Xia Cai<sup>1</sup> and Bang-Gui Liu<sup>2,3</sup>

<sup>1</sup>*School of Electronic Engineering, Xi'an University of Posts and Telecommunications, Xi'an 710121, China*

<sup>2</sup>*Beijing National Laboratory for Condensed Matter Physics, Institute of Physics, Chinese Academy of Sciences, Beijing 100190, People's Republic of China and*

<sup>3</sup>*School of Physical Sciences, University of Chinese Academy of Sciences, Beijing 100190, People's Republic of China*

The valley degrees of freedom of carriers in crystals is useful to process information and perform logic operations, and it is a key factor for valley application to realize the valley polarization. Here, we propose a model that the valley polarization transition at different valley points (-K and K points) is produced by biaxial strain. By the first-principle calculations, we illustrate our idea with a concrete example of Janus GdClF monolayer. The predicted GdClF monolayer is dynamically, mechanically and thermally stable, and is a ferromagnetic (FM) semiconductor with perpendicular magnetic anisotropy (PMA), valence band maximum (VBM) at valley points and high Curie temperature ( $T_C$ ). Due to its intrinsic ferromagnetism and spin orbital coupling (SOC), a spontaneous valley polarization will be induced, but the valley splitting is only -3.1 meV, which provides an opportunity to achieve valley polarization transition at different valley points by strain. In considered strain range ( $a/a_0$ : 0.94~1.06), the strained GdClF monolayer has always energy bandgap, strong FM coupling and PMA. The compressive strain is in favour of -K valley polarization, while the tensile strain makes for K valley polarization. The corresponding valley splitting at 0.96 and 1.04 strain are -44.5 meV and 29.4 meV, which are higher than the thermal energy of room temperature (25 meV). Due to special Janus structure, both in-plane and out-of-plane piezoelectric polarizations can be observed. It is found that the direction of in-plane piezoelectric polarizations can be overturned by strain, and the  $d_{11}$  at 0.96 and 1.04 strain are -1.37 pm/V and 2.05 pm/V. Our works pave the way to design the ferrovalley material as multifunctional valleytronics and piezoelectric devices by strain.

PACS numbers: 71.20.-b, 77.65.-j, 72.15.Jf, 78.67.-n

Email:sandongyuwang@163.com

Keywords: Valleytronics, Ferromagnetism, Piezoelectronics, 2D materials

## I. INTRODUCTION

In analogy to charge and spin of electrons, valley degree of freedom constitutes the binary states in crystals, which lays the foundation for processing information and performing logic operations<sup>1-7</sup>. The valley-related filed is truly flourishing with the advent of two-dimensional (2D) materials. Valley is referred to two or more local energy extremes in the conduction band or valence band. These valleys are degenerate but inequivalent, which are well separated in the 2D momentum space with suppressed intervalley interactions<sup>1</sup>. Nevertheless, to achieve valley application, it is very necessary to realize the valley polarization. The optical pumping, magnetic field, magnetic substrates and magnetic doping have been proposed to induce polarization<sup>8-11</sup>. However, these methods may destroy the intrinsic energy band structures and crystal structures of these valley materials. Then, the 2D magnetic materials provide an opportunity to realize spontaneous valley polarization (namely ferrovalley materials)<sup>12</sup>, and many 2D materials have been predicted with spontaneous valley polarization, such as 2H-VSe<sub>2</sub><sup>12</sup>, CrSi<sub>2</sub>X<sub>4</sub> (X=N and P)<sup>13</sup>, VAgP<sub>2</sub>Se<sub>6</sub><sup>14</sup>, LaBr<sub>2</sub><sup>15,16</sup>, VSi<sub>2</sub>P<sub>4</sub><sup>17</sup>, NbX<sub>2</sub> (X =S and Se)<sup>18</sup>, Nb<sub>3</sub>I<sub>8</sub><sup>19</sup>, TiVI<sub>6</sub><sup>20</sup>, FeClBr<sup>21</sup>.

Although a 2D material is ferrovalley material, its valley splitting may be zero or very little due to accidental factor. Taking 2D hexagonal lattice for example, when compressive/tensile strain is applied, -K/K valley will be

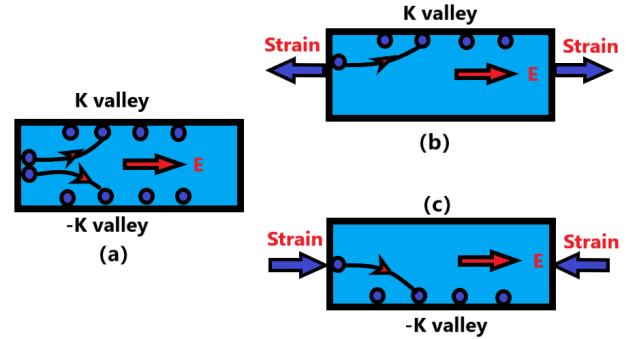


FIG. 1. (Color online) Sketch of strain-induced anomalous valley Hall effect under an in-plane longitudinal electric field  $E$ . (a) Without strain, no valley polarization is produced. (b) With applied tensile strain, the K valley is polarized. (c) With applied compressive strain, the -K valley is polarized.

polarized. When an in-plane longitudinal electric field  $E$  is imposed, the Bloch electrons will acquire an anomalous Hall velocity  $v$  due to  $v \sim E \times \Omega(k)$ <sup>7</sup>, where the  $\Omega(k)$  is Berry curvature. Then, the anomalous valley Hall effect (AVHE) will be produced by the carriers of -K/K valley with compressive/tensile strain. The proposed model is illustrated in Figure 1. Recently, a kind of f-electrons 2D FM semiconductors GdX<sub>2</sub> (X=F, Cl, Br and I) are reported, which possess high Curie temperature<sup>22-24</sup>. The monolayer GdI<sub>2</sub> of them is predicted as a ferrovalley material with a giant splitting of 149 meV<sup>25</sup>. However, GdI<sub>2</sub>

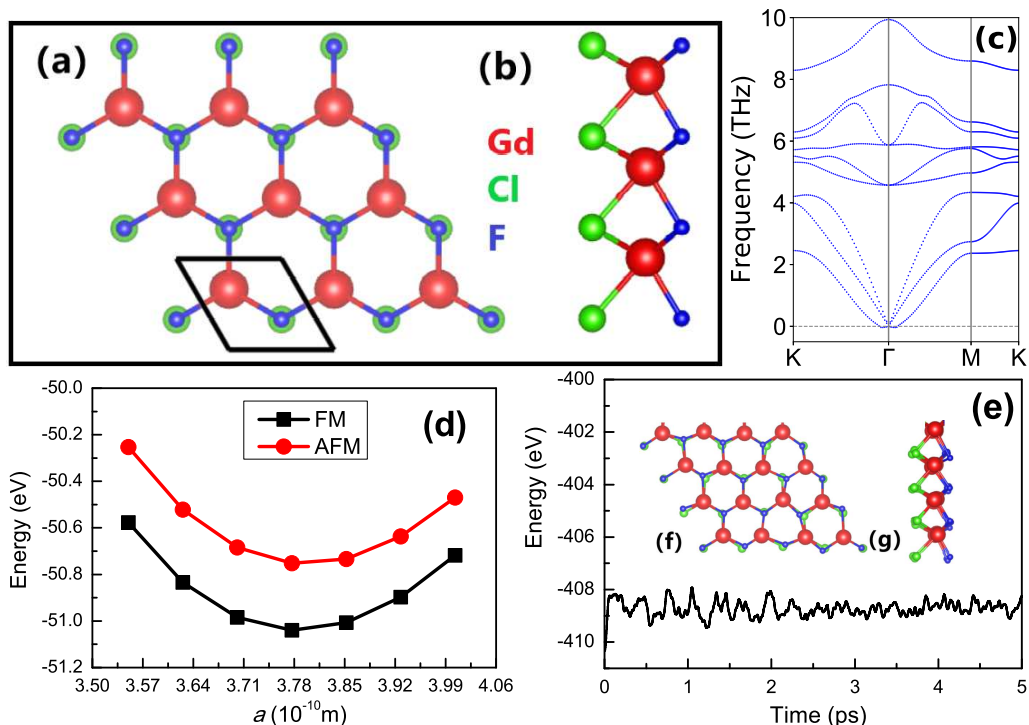


FIG. 2. (Color online) The (a) top view and (b) side view of crystal structure of Janus monolayer GdClF, and the black frame represents the rhombus primitive cell. (c) The phonon dispersions of Janus monolayer GdClF using GGA+U. (d) The FM and AFM energies of Janus monolayer GdClF as a function of lattice constants  $a$  with rectangle supercell. (e) The variation of free energy of Janus monolayer GdClF as a function of simulation time. Insets show the final structures of Janus monolayer GdClF after 5 ps at 300 K (top view (f) and side view (g)).

possesses in-plane magnetic anisotropy, not PMA<sup>23,24</sup>. Because the space group of  $GdX_2$  ( $X=F, Cl, Br$  and  $I$ ) is  $P\bar{6}m2$ , the generators of this space group are threefold rotational symmetry along the  $z$  direction, out-of-plane mirror symmetry and in-plane mirror symmetry. The in-plane magnetization preserves the symmetry, and so the in-plane magnetic calculations with SOC show that the energies of  $-K$  and  $K$  valleys remain almost degenerate<sup>26</sup>. The out-of-plane magnetization violates the out-of-plane mirror symmetry, the SOC effect will remove the degeneracy of  $-K$  and  $K$  valleys<sup>26</sup>. To make  $GdI_2$  monolayer become polarized, an external out-of-plane magnetic field should be applied. Among  $GdX_2$  ( $X=F, Cl, Br$  and  $I$ ) monolayers, the easy axis of monolayer  $GdF_2$  and  $GdCl_2$  are along the out-of-plane direction<sup>22,24</sup>. For  $GdCl_2$ , the  $K$  valley is polarized with the valley splitting of 42.3 meV, and the polarized valley is at  $-K$  point with valley splitting of 47.6 meV for  $GdF_2$ <sup>22</sup>. A compressive strain can decrease the valley splitting of  $GdCl_2$ , and the polarized valley changes from  $K$  point to  $-K$  point at about 0.963 strain<sup>22</sup>.

In light of these factors about monolayer  $GdF_2$  and  $GdCl_2$  mentioned above, the Janus monolayer GdClF may be a ferromagnetic material with negligible valley splitting. In consideration of Janus monolayer  $MoSSe$  from  $MoS_2$ <sup>27,28</sup>, the Janus monolayer GdClF can be synthesized experimentally with similar synthetic technology

based on  $GdCl_2$  monolayer. The broken space inversion symmetry allows GdClF monolayer to become piezoelectric. In this work, we mainly investigate the strain effects on valley physics and piezoelectric properties of monolayer GdClF by the first-principles calculations. The GdClF monolayer is demonstrated to be a room temperature ferromagnetic material with very little valley splitting. The compressive strain can enhance splitting of  $-K$  valley polarization, while the tensile strain can improve the splitting of  $K$  valley polarization. From compressive strain to tensile one, the strain can overturn in-plane piezoelectric polarizations. Our works provide a potential 2D materials to achieve polarization of different valleys tuned by strain.

The rest of the paper is organized as follows. In the next section, we shall give our computational details and methods. In the next few sections, we shall present structure and stability, electronic structure and valley properties, and piezoelectric properties of Janus monolayer GdClF. Finally, we shall give our conclusions.

## II. COMPUTATIONAL DETAIL

We perform the spin-polarized first-principles calculations within density functional theory (DFT)<sup>29</sup>, as implemented in VASP code<sup>30-32</sup> within the projector

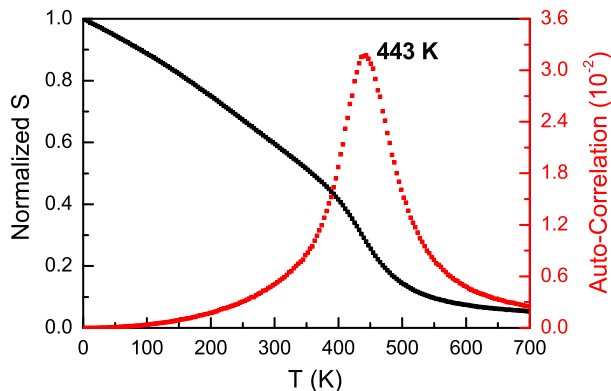


FIG. 3. (Color online) The normalized magnetic moment ( $S$ ) and auto-correlation of Janus monolayer GdClF as a function of temperature.

augmented-wave (PAW) method. The generalized gradient approximation of Perdew-Burke-Ernzerhof (PBE-GGA) functional is adopted as the exchange-correlation functional. The kinetic energy cutoff and total energy convergence criterion is set to 500 eV and  $10^{-8}$  eV, respectively. For optimized convergence criterion, less than  $0.0001 \text{ eV} \cdot \text{\AA}^{-1}$  for force on each atom is used for atomic coordinates. To avoid adjacent interactions, the vacuum space along the out-of-plane direction is set to more than 18  $\text{\AA}$ . We use  $18 \times 18 \times 1$  Monkhorst-Pack k-point mesh to sample the Brillouin zone for calculating electronic structures and elastic properties, and  $10 \times 20 \times 1$  Monkhorst-Pack k-point mesh for piezoelectric calculations. To account for the localized nature of  $4f$  orbitals of Gd atoms, a Hubbard correction  $U_{eff} = 4 \text{ eV}$ <sup>24</sup> is employed within the rotationally invariant approach proposed by Dudarev et al, and the SOC is incorporated for investigation of valley properties.

The elastic stiffness tensor  $C_{ij}$  and piezoelectric stress tensor  $e_{ij}$  are calculated by using strain-stress relationship (SSR) and density functional perturbation theory (DFPT) method<sup>34</sup>, respectively. The 2D elastic coefficients  $C_{ij}^{2D}$  and piezoelectric stress coefficients  $e_{ij}^{2D}$  have been renormalized by  $C_{ij}^{2D} = L_z C_{ij}^{3D}$  and  $e_{ij}^{2D} = L_z e_{ij}^{3D}$ , where the  $L_z$  is the length of unit cell along  $z$  direction. The interatomic force constants (IFCs) of monolayer GdClF are calculated within finite displacement method, and the  $5 \times 5 \times 1$  supercell is used with FM ordering. Based on the harmonic IFCs, phonon dispersion spectrum is attained by the Phonopy code<sup>35</sup>. We use a  $40 \times 40$  supercell and  $10^7$  loops to perform the Monte Carlo (MC) simulations, as implemented in Mcsolver code<sup>36</sup>. The ab initio molecular dynamics (AIMD) simulations using NVT ensemble are performed with a supercell of size  $4 \times 4 \times 1$  for more than 5000 fs with a time step of 1 fs.

### III. STRUCTURE AND STABILITY

The top and side views of crystal structures of the Janus GdClF monolayer are shown in Figure 2 (a and b). The GdClF monolayer consists of Cl-Gd-F sandwich layer, and each Gd atom is surrounded by three Cl and three F atoms forming a triangular prism. The Janus monolayer GdClF can be constructed by replacing one of two Cl (F) layers with F (Cl) atoms in GdCl<sub>2</sub> (GdF<sub>2</sub>) monolayer. Due to missing out-of-plane mirror symmetry, the GdClF monolayer (space group No.156) has lower symmetry compared with GdCl<sub>2</sub>/GdF<sub>2</sub> monolayer (space group No.187). Figure 2 (d) shows the energies of anti-ferromagnetic (AFM) and FM states with rectangle supercell (FIG.1 of electronic supplementary information (ESI)) as a function of lattice constants  $a$ , which implies that the FM order is the most stable magnetic state. The optimized lattice constants with FM order is 3.61  $\text{\AA}$ , which is between ones of GdCl<sub>2</sub> and GdF<sub>2</sub><sup>22,24</sup>. Due to the different atomic sizes and electronegativities of Cl and F atoms, the GdClF monolayer shows the inequivalent Gd-Cl and Gd-F bond lengths (Cl-Gd-Cl and F-Gd-F bond angles), giving rise to a built-in electric field. The corresponding values are 2.772  $\text{\AA}$  and 2.428  $\text{\AA}$  ( $81.27^\circ$  and  $96.02^\circ$ ).

The magnetic anisotropy energy (MAE) can be used to describe magnetic anisotropy of 2D materials, which plays a important role to realize the long-range magnetic ordering. The GdBr<sub>2</sub> and GdI<sub>2</sub> monolayers possess in-plane magnetic anisotropy, but the direction of the easy axis of GdCl<sub>2</sub> and GdF<sub>2</sub> monolayers are out-of-plane ( $z$ -axis)<sup>22-24</sup>. By considering SOC interaction, the MAE is defined by  $E_{MAE} = E_{(100)} - E_{(001)}$ , and the corresponding value is 139  $\mu\text{eV}/\text{Gd}$ . The positive value means that the easy axis of monolayer GdClF is perpendicular to the plane, possessing PMA, as expected.

The Curie temperature  $T_C$  is a key parameter for the practical applications. The  $T_C$  of monolayer GdClF is estimated by using the Wolf MC algorithm based on the Heisenberg model. The spin Heisenberg Hamiltonian can be expressed as:

$$H = -J \sum_{i,j} S_i \cdot S_j - A \sum_i (S_i^z)^2 \quad (1)$$

in which  $S_i$  and  $S_j$  are the spin vectors of each atom, and  $S_i^z$  is the spin component parallel to the  $z$  direction, and  $J$  is the nearest neighbor exchange parameter, and  $A$  represents MAE. The energies ( $E_{FM}$  and  $E_{AFM}$ ) of FM and AFM configurations of monolayer GdClF with rectangle supercell can be written as:

$$E_{FM} = E_0 - 6J|S|^2 - 2A|S|^2 \quad (2)$$

$$E_{AFM} = E_0 + 2J|S|^2 - 2A|S|^2 \quad (3)$$

where  $E_0$  is the total energy of systems without magnetic coupling, and  $|S|$  ( $|S|=4$  for Gd atoms) is the total spin.

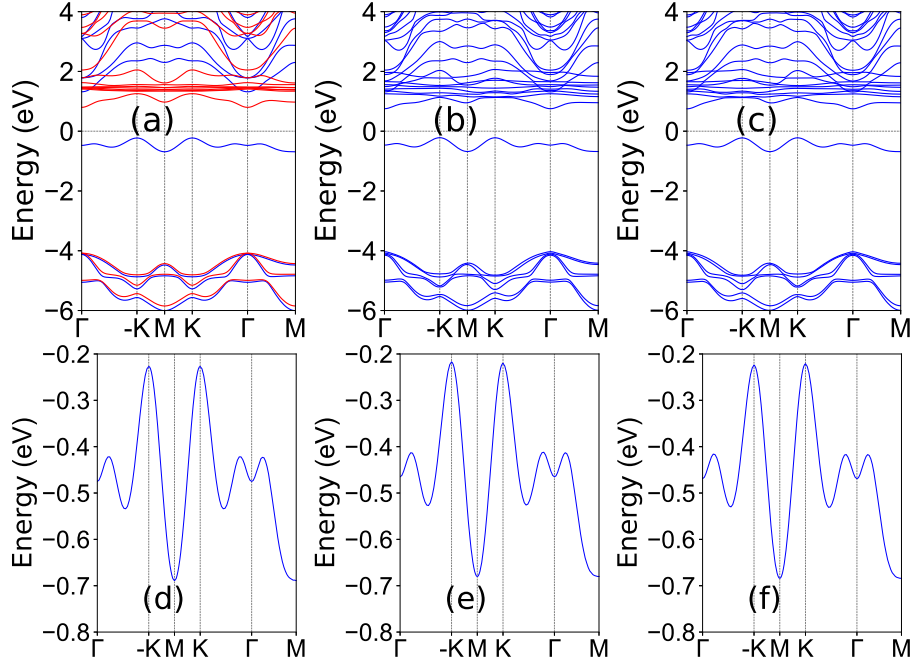


FIG. 4. (Color online) The energy band structures of Janus monolayer GdClF (a) without SOC; (b) and (c) with SOC for magnetic moment of Gd along the positive and negative  $z$  direction, respectively. The (d), (e) and (f) are enlarged views of the valence bands near the Fermi level for (a), (b) and (c). The blue (red) lines represent the band structure in the spin-up (spin-down) direction for (a).

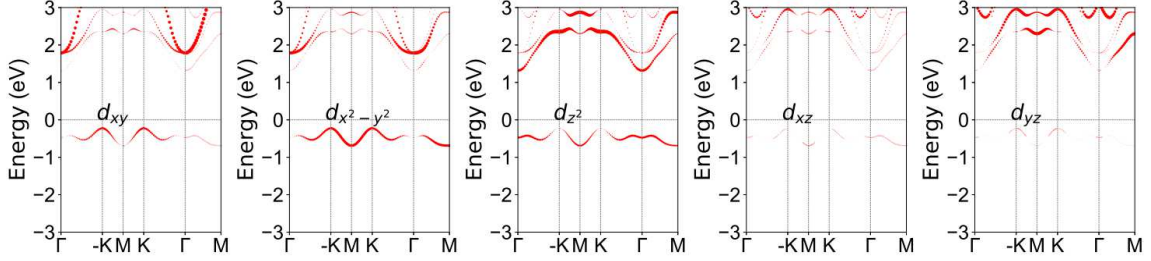


FIG. 5. (Color online) For monolayer GdClF, the Gd- $d$ -orbital characters of energy bands using GGA for spin-up direction.

The nearest neighbor exchange parameter  $J$  is calculated as:

$$J = \frac{E_{AFM} - E_{FM}}{8|S|^2} \quad (4)$$

The calculated  $J$  is 2.244 meV based on  $E_{AFM} - E_{FM} = 287.236$  meV with rectangle supercell. The normalized magnetic moment and auto-correlation of monolayer GdClF vs temperature are shown in Figure 3, and the predicted  $T_C$  is about 443 K. In ref.<sup>24</sup>, the calculated  $J$  of GdCl<sub>2</sub> monolayer is 1.068 meV based on  $E_{AFM} - E_{FM} = 136.8$  meV with rhombus primitive cell, which leads to small  $T_C$  of 224 K<sup>24</sup>.

To demonstrate the dynamical stability of GdClF monolayer, the phonon spectra without imaginary frequency modes are shown in Figure 2 (c). The free energy of Janus monolayer GdClF as a function of simulation time at room temperature is plotted Figure 2 (e), along

with final structures after 5 ps. The free energy shows little oscillation as the time increases, and there is no structural destruction or bond broken during the simulation. These mean that monolayer GdClF is dynamically and thermally stable. To check the mechanical stability of monolayer GdClF, the elastic constants is calculated. Using Voigt notation, the independent elastic constants are  $C_{11}$  and  $C_{12}$  due to hexagonal symmetry. The  $C_{11}$  and  $C_{12}$  are 62.04 Nm<sup>-1</sup> and 17.41 Nm<sup>-1</sup>, which satisfy the Born criteria of mechanical stability<sup>37</sup>:  $C_{11} > 0$  and  $C_{11} - C_{12} > 0$ , confirming the mechanical stability of monolayer GdClF. The monolayer GdClF is mechanically isotropic, so its Young's moduli  $C^{2D}$ , shear modulus  $G^{2D}$  and Poisson's ratios  $\nu^{2D}$  can simply be written as<sup>37</sup>:

$$C^{2D} = \frac{C_{11}^2 - C_{12}^2}{C_{11}} \quad (5)$$

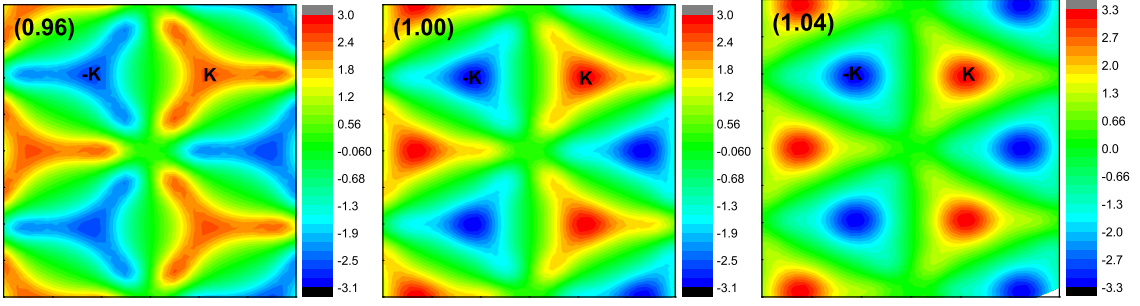


FIG. 6. (Color online) Calculated Berry curvature distribution of Janus monolayer GdClF in the 2D Brillouin zone at 0.96, 1.00 and 1.04 strains.

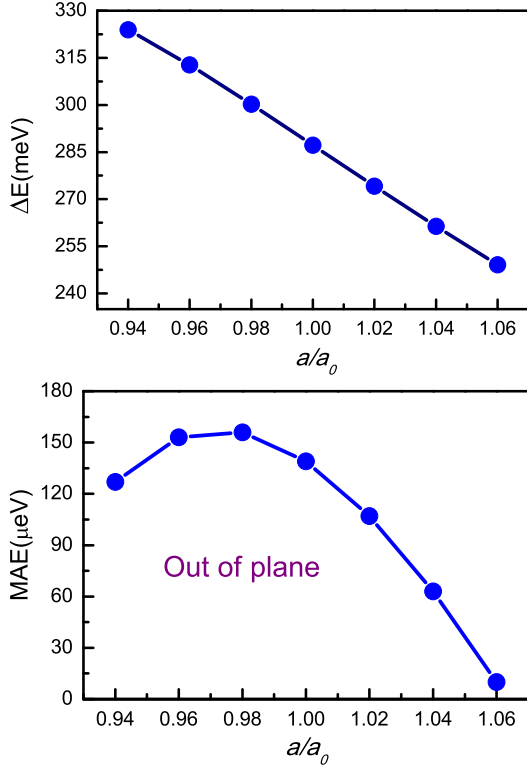


FIG. 7. (Color online) (Top) The energy difference between the AFM and FM states ( $\Delta E$ ) and (Bottom) MAE as a function of the applied biaxial strain  $a/a_0$  for Janus monolayer GdClF.

$$G^{2D} = C_{66} = \frac{C_{11} - C_{12}}{2} \quad (6)$$

$$\nu^{2D} = \frac{C_{12}}{C_{11}} \quad (7)$$

The calculated results show that Young's moduli  $C_{2D}$ , shear modulus  $G_{2D}$  and Poisson's ratio  $\nu$  of GdClF monolayer are  $57.15 \text{ Nm}^{-1}$ ,  $22.32 \text{ Nm}^{-1}$  and 0.281, respectively. The  $C_{2D}$  is less than those of many 2D materials<sup>38,41-45</sup>, which means that GdClF monolayer can be easily tuned by strain.

#### IV. ELECTRONIC STRUCTURE AND VALLEY PROPERTIES

At absence of SOC, the spin-polarized band structure of monolayer GdClF is shown in **Figure 4** (a,d). It is found that GdClF monolayer is an indirect band gap semiconductor with VBM and conduction band minimum (CBM) provided by the spin-up and spin-dn, and they locate at the K and  $\Gamma$  symmetry points with the gap value of 1.025 eV. This means that GdClF monolayer is a bipolar magnetic semiconductor with 100 % spin-polarized currents with inverse spin-polarization direction for electron or hole doping. The monolayer GdClF may be a potential ferrovalley material due to degenerate energy extremes of K and -K high-symmetry points in the valence band (**Figure 4** (d)). The Gd- $d$ -orbital characters of energy bands for spin-up direction are plotted in **Figure 5**. It was clearly seen that the VBM is predominantly contributed by  $d_{x^2-y^2}$  and  $d_{xy}$  orbitals, which is very important to produce valley polarization<sup>12</sup>, when the SOC is included.

With SOC, the energy band structures of monolayer GdClF with magnetic moment of Gd along the positive and negative out-of-plane direction are also plotted in **Figure 4** (b,e and c,f). The SOC effect can induce valley polarization in uppermost valence band (UVB), which is due to the intra-atomic interaction  $\hat{L} \cdot \hat{S}$  ( $\hat{H}_{SOC}^0 + \hat{H}_{SOC}^1 = \lambda \hat{L} \cdot \hat{S}$ ), where  $\hat{L}$  and  $\hat{S}$  represent the orbital angular moment and spin angular moment, respectively. The  $\hat{H}_{SOC}^0$  represents the interaction between the same spin states, which dominates the  $\hat{L} \cdot \hat{S}$ . Due to the magnetic exchange interaction, the opposite spin states interaction ( $\hat{H}_{SOC}^1$ ) can be ignored. The  $\hat{H}_{SOC}^0$  can be expressed as<sup>12,21</sup>:

$$\hat{H}_{SOC}^0 = \lambda \hat{S}_z (\hat{L}_z \cos\theta + \frac{1}{2} \hat{L}_+ e^{-i\phi} \sin\theta + \frac{1}{2} \hat{L}_- e^{+i\phi} \sin\theta) \quad (8)$$

The  $\theta$  and  $\phi$  are the polar angles of spin orientation, which are defined in FIG.1 of ESI. Because the MAE is out-of-plane ( $\theta = 0^\circ$ ),  $\hat{H}_{SOC}^0$  can be simplified as:

$$\hat{H}_{SOC}^0 = \alpha \hat{L}_z \quad (9)$$

The **Equation 9** suggests that the Hamiltonian  $\hat{H}_{SOC}^0$  re-

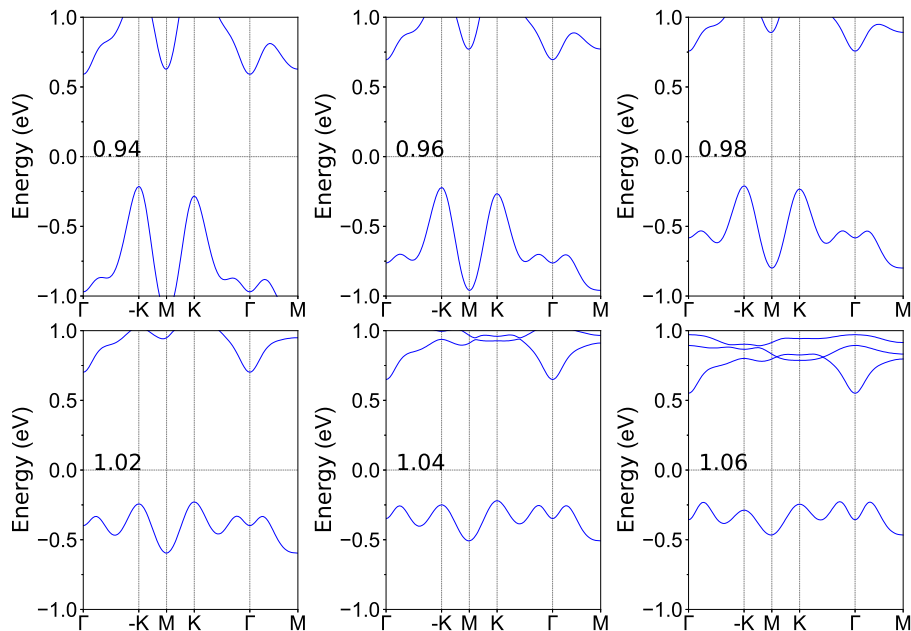


FIG. 8. (Color online) The strained energy band structures of Janus monolayer GdClF with  $a/a_0$  from 0.94 to 1.06 by using GGA+SOC.

lies on the orbital angular momentum  $\hat{L}_z$ . The group symmetry of the wave vector at K and -K points is  $C_{3h}$ , and the basis functions can be expressed as<sup>12,21</sup>:

$$|\phi_\nu^\tau\rangle = \sqrt{\frac{1}{2}}(|d_{x^2-y^2}\rangle + i\tau|d_{xy}\rangle) \quad (10)$$

where the subscript  $\nu$  and  $\tau$  represent valence bands and the valley index ( $\tau = \pm 1$ ). Based on the basis functions, the energy levels of the VBM at K and -K valleys can be expressed as:

$$E_\nu^\tau = \langle \phi_\nu^\tau | \hat{H}_{SOC}^0 | \phi_\nu^\tau \rangle \quad (11)$$

Then, the valence energy difference  $\Delta E_\nu$  of valley at -K and K points (valley splitting) can be expressed as:

$$\Delta E_\nu = E_\nu^K - E_\nu^{-K} = 4\alpha \quad (12)$$

The DFT calculated results show that the  $\Delta E_\nu$  is only -3.1 meV, which means that the energy of K valley state is lower than one of -K valley (Figure 4 (e)). By applying an external magnetic field, the valley polarization of monolayer GdClF can change from -K point to K point. The reversing magnetization of Gd atoms can simultaneously flip the spin and valley polarization, and the energy of K valley will become higher than one of -K valley (Figure 4 (f)), which suggests that the valley polarization can be tuned by the magnetization orientation. This can be explained by  $\Delta E_\nu = 4\alpha \cos\theta$ <sup>21</sup>, when considering the magnetization orientation ( $\theta$  changes from  $0^\circ$  to  $180^\circ$ ). When the magnetization orientation is along in-plane direction ( $\theta=90^\circ$ ), the valley splitting will disappear ( $\Delta E_\nu=0$ ). So, it is a key factor for valley application

to possess PMA. The UVB related with valley polarization is separated well from other energy bands, which is very useful to manipulate valley states.

The electronic transport properties and various Hall effects are related with Berry curvature. Due to broken space inversion symmetry and exchange interaction for hexagonal systems, the carriers will attain a nonzero unequivalent Berry curvature at K and -K valleys, which can induce AVHE<sup>12</sup>. The Berry curvature of GdClF monolayer is calculated directly from the calculated wave functions based on Fukui's method<sup>46</sup>, as implemented in the VASPBERRY code. The calculated Berry curvature distribution in the 2D Brillouin zone with SOC for magnetic moment of Gd along the positive z direction is plotted in Figure 6. It is found that the Berry curvatures of K and -K valleys have opposite signs, and the absolute values are different, giving rise to the typical valley contrasting properties.

For GdCl<sub>2</sub> monolayer, a compressive strain can reduce the valley splitting, and the valley splitting will change sign at about 0.963 strain<sup>22</sup>. The valley splitting  $\Delta E_\nu$  of unstrained GdClF is very small, which provides a possibility to achieve valley polarization at different valley points by tensile and compressive strains. We use  $a/a_0$  to simulate the biaxial strain, where  $a$  and  $a_0$  are the strained and unstrained lattice constants. The  $a/a_0 < 1$  means the compressive strain, and the  $a/a_0 > 1$  represents the tensile strain. Firstly, we determine the magnetic ground state of strained GdClF monolayer by the energy differences of AFM with respect to FM state vs  $a/a_0$ , which is shown in Figure 7. In considered strain range, the DFT calculated results show that the energy difference is always positive, and monotonically decreases

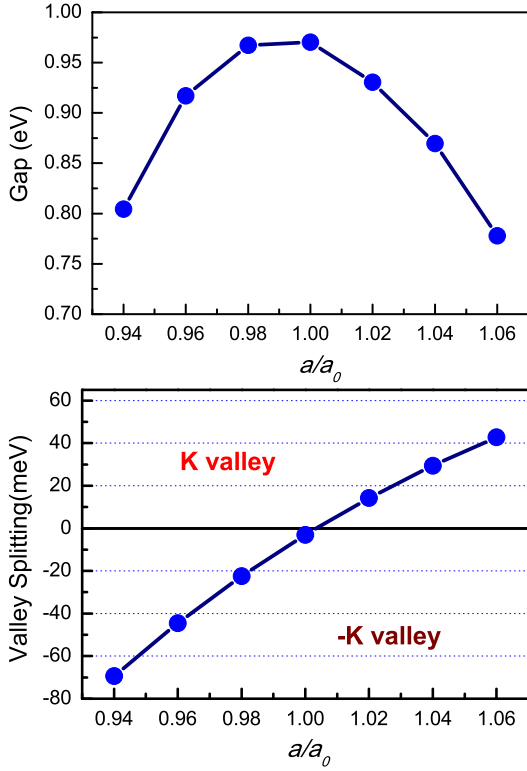


FIG. 9. (Color online) (Top) The energy band gap (Gap) and (Bottom) valley splitting as a function of the applied biaxial strain  $a/a_0$  for Janus monolayer GdClF.

with  $a/a_0$  from 0.94 to 1.06. This confirms the FM ground state of strained monolayer GdClF in considered strain range. It is found that the compressive strain can strengthen the FM coupling between Gd atoms, while the tensile strain can reduce the FM coupling. Another factor is to confirm PMA of strained GdClF monolayer to possess stable long-range magnetic ordering without external field. The MAE as a function of  $a/a_0$  is also plotted in Figure 7, which shows a decrease with increasing  $a/a_0$ . However, the MAE is always positive, which means that the easy axis of strained monolayer GdClF is always along  $z$  direction.

The energy band structures of strained monolayer GdClF by using GGA+SOC are plotted in Figure 8, and the corresponding energy band gaps are shown in Figure 9. The strained monolayer GdClF is always an indirect gap semiconductor, and the CBM maintains at  $\Gamma$  point. For VBM, the tensile strain (about 1.06) can change it from K/-K point to one point along (K/-K)- $\Gamma$  path. The energy band gap firstly increases, and then decreases, when the strain changes from compressive one to tensile one. Similar phenomenon can be found in many 2D materials<sup>39,40</sup>. The valley splitting vs  $a/a_0$  is also plotted in Figure 9. The compressive strain can make the absolute value of valley splitting become large, inducing -K valley polarization. However, the increasing tensile strain enhances the valley splitting, giving rise to

TABLE I. For monolayer GdF<sub>2</sub><sup>22</sup>, GdClF and GdCl<sub>2</sub><sup>22</sup>, the elastic constants  $C_{ij}$  in Nm<sup>-1</sup>, the piezoelectric stress coefficients  $e_{11}/e_{31}$  in 10<sup>-10</sup> C/m, and the piezoelectric strain coefficients  $d_{11}/d_{31}$  in pm/V.

Name	$C_{11}$	$C_{12}$	$e_{11}$	$e_{31}$	$d_{11}$	$d_{31}$
GdF <sub>2</sub>	73.87	19.61	0.317	-	0.584	-
GdClF	62.04	17.41	-0.260	-0.181	-0.583	-0.228
GdCl <sub>2</sub>	45.95	13.53	-0.878	-	-2.708	-

K valley polarization. At moderate 0.96 and 1.04 strain, the corresponding valley splitting are -44.5 meV and 29.4 meV, which are larger than the thermal energy of room temperature (25 meV). This is very important for room-temperature electronic device. The Berry curvature distributions of monolayer GdClF at 0.96 and 1.04 strains by using GGA+SOC are plotted in Figure 6. With increasing  $a/a_0$ , the Berry curvatures (absolute value) of two valleys increase slightly. Due to small Young's moduli  $C_{2D}$  of GdClF monolayer, the 0.96 and 1.04 strains can be easily achieved experimentally. These confirm the achievement of different valley polarization by strain.

## V. PIEZOELECTRIC PROPERTIES

The ferrovalley materials should break inversion symmetry, which means that they are piezoelectric. The piezoelectric effects of a material can be described by third-rank piezoelectric stress tensor  $e_{ijk}$  and strain tensor  $d_{ijk}$ , which can be attained from the sum of ionic and electronic parts. They are defined as:

$$e_{ijk} = \frac{\partial P_i}{\partial \varepsilon_{jk}} = e_{ijk}^{elc} + e_{ijk}^{ion} \quad (13)$$

and

$$d_{ijk} = \frac{\partial P_i}{\partial \sigma_{jk}} = d_{ijk}^{elc} + d_{ijk}^{ion} \quad (14)$$

Where  $P_i$ ,  $\varepsilon_{jk}$  and  $\sigma_{jk}$  are polarization vector, strain and stress, respectively. The  $e_{ijk}^{elc}/d_{ijk}^{elc}$  is clamped-ion piezoelectric coefficients, not including ionic contribution. The  $e_{ijk}/d_{ijk}$  is relax-ion piezoelectric coefficients as a realistic result.

For GdClF monolayer, it not only lacks inversion symmetry, but also breaks vertical mirror symmetry. This is different from monolayer GdCl<sub>2</sub>, whose vertical mirror symmetry still holds. These mean that the piezoelectric coefficients  $e_{11}/d_{11}$  and  $e_{31}/d_{31}$  of GdClF monolayer are nonzero. This is the same with ones of Janus monolayer MoSSe<sup>41</sup>. For 2D materials, by using Voigt notation with only considering the in-plane strain and stress<sup>41-45</sup>, the piezoelectric stress, strain and elastic tensors can be re-

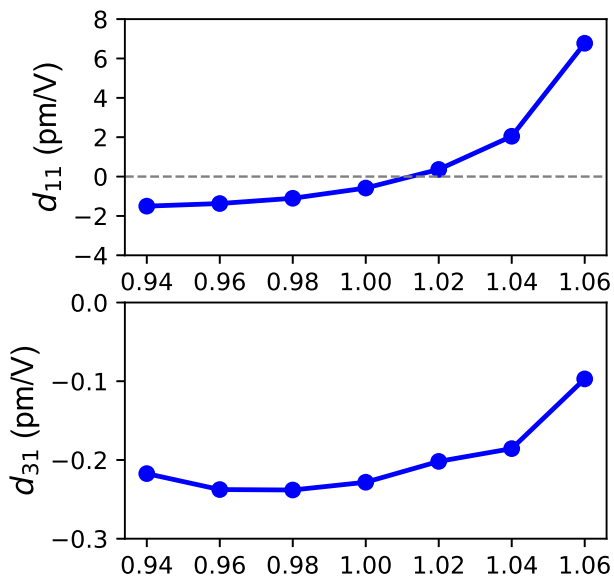


FIG. 10. (Color online) For monolayer GdClF, the piezoelectric strain coefficient ( $d_{11}$  and  $d_{31}$ ) as a function of  $a/a_0$ .

duced into:

$$e = \begin{pmatrix} e_{11} & -e_{11} & 0 \\ 0 & 0 & -e_{11} \\ e_{31} & e_{31} & 0 \end{pmatrix} \quad (15)$$

$$d = \begin{pmatrix} d_{11} & -d_{11} & 0 \\ 0 & 0 & -2d_{11} \\ d_{31} & d_{31} & 0 \end{pmatrix} \quad (16)$$

$$C = \begin{pmatrix} C_{11} & C_{12} & 0 \\ C_{12} & C_{11} & 0 \\ 0 & 0 & (C_{11} - C_{12})/2 \end{pmatrix} \quad (17)$$

With an imposed uniaxial in-plane strain, the in-plane and out of plane piezoelectric polarization ( $e_{11}/d_{11}$  and  $e_{31}/d_{31} \neq 0$ ) can be induced. However, when a biaxial in-plane strain is applied, the in-plane piezoelectric response will be suppressed ( $e_{11}/d_{11} = 0$ ), but the out of plane piezoelectric polarization still can be induced ( $e_{31}/d_{31} \neq 0$ ). The  $d_{11}$  and  $d_{31}$  can be calculated by  $e_{ik} = d_{ij}C_{jk}$ :

$$d_{11} = \frac{e_{11}}{C_{11} - C_{12}} \quad \text{and} \quad d_{31} = \frac{e_{31}}{C_{11} + C_{12}} \quad (18)$$

The orthorhombic supercell is used to calculate the  $e_{11}/e_{31}$  of monolayer GdClF by using DFPT method. The calculated  $e_{11}/e_{31}$  is  $-0.260 \times 10^{-10} / -0.181 \times 10^{-10}$  C/m with ionic part  $-1.558 \times 10^{-10} / -0.276 \times 10^{-10}$  C/m and electronic part  $1.298 \times 10^{-10} / 0.095 \times 10^{-10}$  C/m. The electronic and ionic contributions of both  $e_{11}$  and  $e_{31}$

have opposite signs, and the ionic part dominates the piezoelectricity. Based on Equation 18, the calculated  $d_{11}$  and  $d_{31}$  are  $-0.583$  and  $-0.228$  pm/V. The  $\text{GdX}_2$  ( $X = \text{Cl}$  and  $\text{F}$ ) monolayers have been predicted, and they possess only in-plane piezoelectricity<sup>22</sup>. The data related with elastic and piezoelectric properties of monolayer  $\text{GdF}_2$ ,  $\text{GdClF}$  and  $\text{GdCl}_2$  are summarized in Table I. It is found that the  $d_{11}$  (absolute value) of monolayer  $\text{GdClF}$  is smaller than one of  $\text{GdCl}_2$ , and is almost the same with one of  $\text{GdF}_2$ .

The strain effects on piezoelectric properties of monolayer  $\text{GdClF}$  are investigated. The elastic constants ( $C_{11}$ ,  $C_{12}$ ,  $C_{11}-C_{12}$  and  $C_{11}+C_{12}$ ) and piezoelectric stress coefficients ( $e_{11}$  and  $e_{31}$ ) along the ionic and electronic contributions of monolayer  $\text{GdClF}$  as a function of  $a/a_0$  are plotted in FIG.2 and FIG.3 of ESI. The  $d_{11}$  and  $d_{31}$  vs  $a/a_0$  are plotted in Figure 10. In the considered strain range, all strained monolayer  $\text{GdClF}$  are mechanically stable, because the calculated elastic constants all satisfy the mechanical stability criteria<sup>37</sup>. With  $a/a_0$  from 0.94 to 1.06, the  $d_{11}$  changes from negative value to positive one at about 1.015 strain, which mainly depends on  $e_{11}$ . When  $a/a_0$  is less than about 1.05, the ionic and electronic parts have opposite contributions to  $e_{11}$ . At 1.06, a very large  $d_{11}$  (6.77 pm/V) is observed, which is mainly due to superimposed contribution from the ionic and electronic parts. The  $d_{31}$  (absolute value) shows a decreasing trend with strain from compressive one to tensile one. At 0.96 and 1.04 strains, the  $d_{11}$  of monolayer  $\text{GdClF}$  are  $-1.37$  pm/V and  $2.05$  pm/V, which provides the possibility for the combination of valley properties and piezoelectricity.

## VI. CONCLUSION

In summary, we present a model for valleytronics to induce polarization of different valley points. We demonstrate our ideas by a concrete 2D material  $\text{GdClF}$  by first-principles calculations. Monolayer  $\text{GdClF}$  is predicted to be a FM semiconductor with a pair of valleys locating at the K and  $-\text{K}$  points, and possess PMA and high  $T_C$ . Due to the intrinsic magnetic interaction and SOC, the valley splitting between K and  $-\text{K}$  valleys can be induced, but the value is very little. By imposed increasing compressive strain, the  $-\text{K}$  valley polarization is produced with enhanced valley splitting. On the contrary, the valley splitting is improved for K valley polarization, when the tensile strain increases. Additionally, the piezoelectric properties of monolayer  $\text{GdClF}$  are also studied. It is found that the strain can reverse the direction of in-plane piezoelectric polarizations, when the strain changes from compressive one to tensile one. Our works predict Janus monolayer  $\text{GdClF}$  with the combination of valley properties and piezoelectricity. Moreover, the valley polarization and in-plane piezoelectric polarizations can be effectively tuned by strain. These offer a great potential application in next-generation multifunctional devices.



## ACKNOWLEDGMENTS

This work is supported by Natural Science Basis Research Plan in Shaanxi Province of China (2021JM-

456). We are grateful to the Advanced Analysis and Computation Center of China University of Mining and Technology (CUMT) for the award of CPU hours and WIEN2k/VASP software to accomplish this work.

- 
- <sup>1</sup> J. R. Schaibley, H. Yu, G. Clark, P. Rivera, J. S. Ross, K. L. Seyler, W. Yao, and X. Xu, *Nat. Rev. Mater.* **1**, 16055 (2016).
- <sup>2</sup> G. Pacchioni, *Nat. Rev. Mater.* **5**, 480 (2020).
- <sup>3</sup> S. A. Vitale, D. Nezhich, J. O. Varghese, P. Kim, N. Gedik, P. Jarillo-Herrero, D. Xiao, and M. Rothschild, *Small* **14**, 1801483 (2018).
- <sup>4</sup> D. Xiao, G. B. Liu, W. Feng, X. Xu, and W. Yao, *Phys. Rev. Lett.* **108**, 196802 (2012).
- <sup>5</sup> W. Yao, D. Xiao, and Q. Niu, *Phys. Rev. B* **77**, 235406 (2008).
- <sup>6</sup> D. Xiao, W. Yao, and Q. Niu, *Phys. Rev. Lett.* **99**, 236809 (2007).
- <sup>7</sup> D. Xiao, M. C. Chang, and Q. Niu, *Rev. Mod. Phys.* **82**, 1959 (2010).
- <sup>8</sup> H. Zeng, J. Dai, W. Yao, D. Xiao and X. Cui, *Nat. Nanotechnol.* **7**, 490 (2012).
- <sup>9</sup> D. MacNeill, C. Heikes, K. F. Mak, Z. Anderson, A. Kormányos, V. Zólyomi, J. Park and D. C. Ralph, *Phys. Rev. Lett.* **114**, 037401 (2015).
- <sup>10</sup> C. Zhao, T. Norden, P. Zhang, P. Zhao, Y. Cheng, F. Sun, J. P. Parry, P. Taheri, J. Wang, Y. Yang, T. Scrace, K. Kang, S. Yang, G. Miao, R. Sabirianov, G. Kioseoglou, W. Huang, A. Petrou and H. Zeng, *Nat. Nanotechnol.* **12**, 757 (2017).
- <sup>11</sup> M. Zeng, Y. Xiao, J. Liu, K. Yang and L. Fu, *Chem. Rev.* **118**, 6236 (2018).
- <sup>12</sup> W. Y. Tong, S. J. Gong, X. Wan, and C. G. Duan, *Nat. Commun.* **7**, 13612 (2016).
- <sup>13</sup> Y. B. Liu, T. Zhang, K. Y. Dou, W. H. Du, R. Peng, Y. Dai, B. B. Huang, and Y. D. Ma, *J. Phys. Chem. Lett.* **12**, 8341 (2021).
- <sup>14</sup> Z. Song, X. Sun, J. Zheng, F. Pan, Y. Hou, M.-H. Yung, J. Yang, and J. Lu, *Nanoscale* **10**, 13986 (2018).
- <sup>15</sup> J. Zhou, Y. P. Feng, and L. Shen, *Phys. Rev. B* **102**, 180407(R) (2020).
- <sup>16</sup> P. Zhao, Y. Ma, C. Lei, H. Wang, B. Huang, and Y. Dai, *Appl. Phys. Lett.* **115**, 261605 (2019).
- <sup>17</sup> X. Y. Feng, X. L. Xu, Z. L. He, R. Peng, Y. Dai, B. B. Huang and Y. D. Ma, *Phys. Rev. B* **104**, 075421 (2021)
- <sup>18</sup> Y. Zang, Y. Ma, R. Peng, H. Wang, B. Huang, and Y. Dai, *Nano Res.* **14**, 834 (2021).
- <sup>19</sup> R. Peng, Y. Ma, X. Xu, Z. He, B. Huang, and Y. Dai, *Phys. Rev. B* **102**, 035412 (2020).
- <sup>20</sup> W. Du, Y. Ma, R. Peng, H. Wang, B. Huang, and Y. Dai, *J. Mater. Chem. C* **8**, 13220 (2020).
- <sup>21</sup> R. Li, J. W. Jiang, W. B. Mi and H. L. Bai, *Nanoscale* **13**, 14807 (2021).
- <sup>22</sup> S. D. Guo, J. X. Zhu, W. Q. Mu and B. G. Liu, arXiv:2109.13534 (2021)
- <sup>23</sup> B. Wang, X. W. Zhang, Y. H. Zhang, S. J. Yuan, Y. L. Guo, S. Dong and J. L. Wang, *Mater. Horiz.* **7**, 1623 (2020).
- <sup>24</sup> W. Q. Liu, J. W. Tong, L. Deng, B. Yang, G. M. Xie, G. W. Qin, F. B. Tian, X. M. Zhang, *Materials Today Physics* **21**, 100514 (2021).
- <sup>25</sup> H. X. Cheng, J. Zhou, W. Ji, Y. N. Zhang and Y. P. Feng, *Phys. Rev. B* **103**, 125121 (2021).
- <sup>26</sup> X. R. Kong, L. Y. Li, L. B. Liang, F. M. Peeters and X. J. Liu, *Appl. Phys. Lett.* **116**, 192404 (2020).
- <sup>27</sup> A.-Y. Lu, H. Zhu, J. Xiao, C.-P. Chuu, Y. Han, M.-H. Chiu, C.-C. Cheng, C.-W. Yang, K.-H. Wei, Y. Yang, Y. Wang, D. Sokaras, D. Nordlund, P. Yang, D. A. Muller, M.-Y. Chou, X. Zhang and L.-J. Li, *Nat. Nanotechnol.* **12**, 744 (2017).
- <sup>28</sup> J. Zhang, S. Jia, I. Kholmanov, L. Dong, D. Er, W. Chen, H. Guo, Z. Jin, V. B. Shenoy, L. Shi and J. Lou, *ACS Nano* **11**, 8192 (2017).
- <sup>29</sup> P. Hohenberg and W. Kohn, *Phys. Rev.* **136**, B864 (1964); W. Kohn and L. J. Sham, *Phys. Rev.* **140**, A1133 (1965).
- <sup>30</sup> G. Kresse, *J. Non-Cryst. Solids* **193**, 222 (1995).
- <sup>31</sup> G. Kresse and J. Furthmüller, *Comput. Mater. Sci.* **6**, 15 (1996).
- <sup>32</sup> G. Kresse and D. Joubert, *Phys. Rev. B* **59**, 1758 (1999).
- <sup>33</sup> J. P. Perdew, K. Burke and M. Ernzerhof, *Phys. Rev. Lett.* **77**, 3865 (1996).
- <sup>34</sup> X. Wu, D. Vanderbilt and D. R. Hamann, *Phys. Rev. B* **72**, 035105 (2005).
- <sup>35</sup> A. Togo, F. Oba, and I. Tanaka, *Phys. Rev. B* **78**, 134106 (2008).
- <sup>36</sup> L. Liu, X. Ren, J. H. Xie, B. Cheng, W. K. Liu, T. Y. An, H. W. Qin and J. F. Hu, *Appl. Surf. Sci.* **480**, 300 (2019).
- <sup>37</sup> E. Cadelano and L. Colombo, *Phys. Rev. B* **85**, 245434 (2012).
- <sup>38</sup> C. Lee, X. Wei, J. W. Kysar and J. Hone, *Science* **321**, 385 (2008).
- <sup>39</sup> S. D. Guo and J. Dong, *Semicond. Sci. Tech.* **33**, 085003 (2018).
- <sup>40</sup> S. D. Guo, *J. Mater. Chem. C* **4**, 9366 (2016).
- <sup>41</sup> L. Dong, J. Lou and V. B. Shenoy, *ACS Nano*, **11**, 8242 (2017).
- <sup>42</sup> M. N. Blonsky, H. L. Zhuang, A. K. Singh and R. G. Hennig, *ACS Nano*, **9**, 9885 (2015).
- <sup>43</sup> S. D. Guo, Y. T. Zhu, W. Q. Mu and W. C. Ren, *EPL* **132**, 57002 (2020).
- <sup>44</sup> S. D. Guo, Y. T. Zhu, W. Q. Mu, L. Wang and X. Q. Chen, *Comp. Mater. Sci.* **188**, 110223 (2021).
- <sup>45</sup> K. N. Duerloo, M. T. Ong and E. J. Reed, *J. Phys. Chem. Lett.* **3**, 2871 (2012).
- <sup>46</sup> T. Fukui, Y. Hatsugai and H. Suzuki, *J. Phys. Soc. Japan.* **74**, 1674 (2005).